Fusion Engineering and Design 171 (2021) 112706

Contents lists available at ScienceDirect

Fusion Engineering and Design

journal homepage: www.elsevier.com/locate/fusengdes

Magnetic equilibrium design for the SMART tokamak

S.J. Doyle [*,a,b], D. Lopez-Aires [a,b], A. Mancini [a,b], M. Agredano-Torres [b], J.L. Garcia-Sanchez [b], J. Segado-Fernandez [d], J. Ayllon-Guerola [c,b], M. Garcia-Muñoz [a,b], E. Viezzer [a,b], C. Soria-Hoyo [d], J. Garcia-Lopez [a,b], G. Cunningham [e], P.F. Buxton [f], M.P. Gryaznevich [f], Y.S. Hwang [g], K. J. Chung [g]

[a] Dept. of Atomic, Molecular and Nuclear Physics, University of Seville, Seville, Spain
[b] Centro Nacional de Aceleradores, (U. Seville, CSIC, J. de Andalusia), Seville, Spain
[c] Dept. of Mechanical Engineering and Manufacturing, University of Seville, Seville, Spain
[d] Dept. of Electronics and Electromagnetism, University of Seville, Seville, Spain
[e] Culham Centre for Fusion Energy, Culham Science Centre, Abingdon OX14 3EB, UK
[f] Tokamak Energy Ltd, 173 Brook Drive Milton Park Abingdon OX14 4SD UK
[g] Department of Nuclear Engineering, Seoul National University, Seoul 151-742, Korea

ARTICLE INFO

Keywords:
Spherical tokamak
Equilibrium
Null-field
Breakdown
SMART

ABSTRACT

The *SMall Aspect Ratio Tokamak* (SMART) device is a new compact (plasma major radius $R_{geo} \geq 0.40$ m, minor radius $a \geq 0.20$ m, aspect ratio $A \geq 1.7$) spherical tokamak, currently in development at the University of Seville. The SMART device has been designed to achieve a magnetic field at the plasma center of up to $B_\phi = 1.0$ T with plasma currents up to $I_p = 500$ kA and a pulse length up to $\tau_{ft} = 500$ ms. A wide range of plasma shaping configurations are envisaged, including triangularities between $-0.50 \leq \delta \leq 0.50$ and elongations of $\kappa \leq 2.25$. Control of plasma shaping is achieved through four axially variable poloidal field coils (PF), and four fixed divertor (Div) coils, nominally allowing operation in lower-single null, upper-single null and double-null configurations. This work examines phase 2 of the SMART device, presenting a baseline reference equilibrium and two highly-shaped triangular equilibria. The relevant PF and Div coil current waveforms are also presented. Equilibria are obtained via an axisymmetric Grad-Shafranov force balance solver (Fiesta), in combination with a circuit equation rigid current displacement model (RZIp) to obtain time-resolved vessel and plasma currents.

1. Introduction

Spherical tokamaks (ST) are a sub-class of magnetic fusion devices notable for their narrow radial extent, hence reduced aspect ratios, and represent a promising economic path to commercial fusion due to their compact form, cost-effectiveness and high power density [1–3]. In the three decades since their conception with the START device [4–6] numerous ST have been designed and operated, including but not limited to: MAST [7,8], NSTX [9], Pegasus [10,11], Globus-M [12] & Globus-M2 [13], QUEST [14,15], LATE [16], LTX [17,18], ST40 [19, 20], SUNIST [21,22], TST-2 [23,24] and VEST [25,26]. The aggregated findings from these, and other ST devices have shown encouraging results including; high bootstrap current fractions [1,5], enhanced stability to pressure driven instabilities [2] and reduced particle-driven instabilities [27] as compared to traditional high-aspect ratio designs. These benefits are typically attributed to an enhanced plasma-β, and are also thought to arise from strong toroidal flow and flow shear present in such low aspect ratio plasmas [28,29].

Over the past couple of decades there has emerged a significant interest in plasma shaping within magnetically confined devices, which is known to influence the plasma pressure and current limits [30]. Of the possible shaping parameters; plasma elongation, being the height of the plasma column divided by the width, and triangularity, being the ratio between the highest/lowest vertical extent of the plasma column and the minor radius, have been the most extensively examined. Highly elongated and triangular plasma cross-sections have been found to positively impact the energy confinement time, electron heat transport and edge stability in L and H-mode plasmas [31–34]. In particular, plasma discharges with negative triangularity have recently been demonstrated to achieve H-mode-like confinement characteristics in the absence of an

* Corresponding author at: Dept. of Atomic, Molecular and Nuclear Physics, University of Seville, Seville, Spain.
E-mail addresses: scott.doyle@physics.org, doyle-ext@us.es (S.J. Doyle).

https://doi.org/10.1016/j.fusengdes.2021.112706
Received 29 November 2020; Received in revised form 15 May 2021; Accepted 26 May 2021
Available online 14 June 2021

edge pressure pedestal [31,35]. To date, the majority of this work has been performed in mid-to-large size traditional high-aspect ratio tokamaks, with the effects of negative triangularities on plasma properties in STs remaining largely unknown.

To aid in addressing these issues, a novel compact spherical tokamak named the *SMall Aspect Ratio Tokamak* (SMART) is being designed at the University of Seville to serve as a low-cost, versatile and educational fusion research device [36,37]. The SMART device is designed to accommodate a plasma of major radius $R_{geo} \geq 0.4$ m and minor radius $a \geq 0.2$ m, achieving aspect ratios of $A \geq 1.7$, while simultaneously achieving highly elongated ($\kappa \leq 2.25$) and highly triangular ($-0.50 \leq \delta \leq +0.50$) plasma cross-sections.

SMART's mission goals will address: plasma transport and confinement in positive and negative triangularities, the effect of shear flow velocity on edge plasma turbulence, MHD stability and the control of energetic particle losses in high β plasmas. The SMART device will also serve as a platform for the development of novel diagnostic techniques, divertor configurations, plasma facing materials and control schemes, while also facilitating the training of the next generation of fusion physicists and engineers.

This paper presents an outline of the SMART device and key target parameters of developmental phases 1–3, before focusing on the modelling of three (phase 2) high-shaped equilibria, including an analysis of the breakdown thresholds and associated coil current waveforms for each scenario. An overview of the SMART device is given in Section 2 and descriptions of the numerical methods employed are provided in Section 3. The solenoid, poloidal field and divertor coil current waveforms for the baseline phase 2 operational scenario are outlined in Section 4.1, while the optimised vacuum magnetic field topology and associated breakdown conditions are discussed in Section 4.2. Finally, the high-performance baseline and shaped equilibria are presented in Section 4.3. A summary is given in Section 5.

2. SMART device characteristics

An overview of the SMART device is shown in Fig. 1(a), illustrating the vaccum vessel in grey, toroidal field coils (TFC) in orange, poloidal field coils (PFC) and divertor coils (Div) are shown in yellow and the central solenoid (Sol) in red. Fig. 1(b) shows the associated simulation domain employed in this work, corresponding to an axis-symmetric 2D cross-section of the torus, and is discussed in more detail with regards to the numerical model in Section 3.

The SMART device consists of a 0.8 m radius by 1.6 m height stainless steel (AISI 316 L) vacuum vessel [36], with a total internal volume of 3.1 m^3. To minimise eddy current formation the vessel employs a 4 mm thick inboard wall and 8 mm thick outboard wall, with two more substantial 15 mm thick upper and lower lids, bolted to the vessel to enable maintenance access. Further diagnostic access is provided by 36 circular ports, positioned radially, dorsally and ventrally, and 2 larger rectangular ports, positioned radially. Thermal protection is provided by carbon tiles affixed to the inboard wall, and poloidal limiters (not shown). The vacuum system comprises 4 pumps including two dry 80 m^{3}h^{-1} pumps and two turbomolecular 2000 ls^{-1} pumps, capable of achieving a vacuum of 1.33×10^{-6} Pa (10^{-8} Torr).

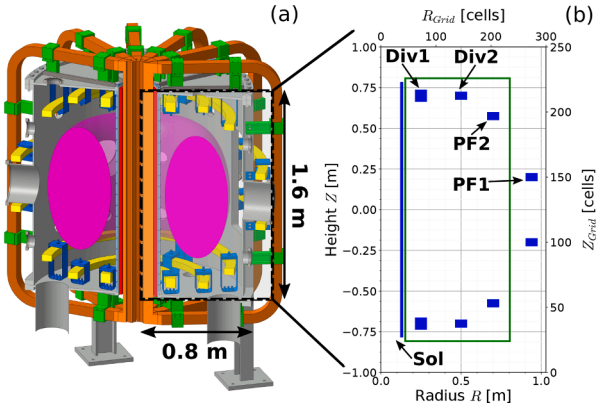

Fig. 1. Overview of the SMART device showing (a) a 3D cutaway of the vessel and coil geometry and (b) the 2D axis-symmetric mesh employed in this work. The vacuum vessel is shown in grey, toroidal field coils (TFC) in orange, poloidal field coils (PFC) and divertor coils (Div) in yellow, solenoid (Sol) in red and supports in blue and green. (For interpretation of the references to colour in this figure legend, the reader is referred to the web version of this article.)

The toroidal field is provided by a set of twelve TFC, comprised of 48, 35 × 35 mm, square cross-section windings, decreasing to 21 × 21 mm cross-section for the inboard limbs. Two pairs of axially variable PFC sets provide plasma shaping and control, comprising 23, 11 × 11 mm, windings and where the PF1 coil set is positioned external to the vessel to maximise the internal plasma volume. Two pairs of fixed Div coil sets enable operation in either an upper or lower single-null or a double-null configuration. The Div1 set comprises a larger 35 winding construction, utilizing the same 11 × 11 mm winding cross-section, while the Div2 coil set is constructed in the same fashion as the PFC, and also serves as the vertical control feedback coil. All windings comprise a central hollow tube, enabling active water cooling and reducing the number of internal vacuum seals.

Plasma startup and ohmic heating is provided by a central 1.55 m tall, 0.12 m inner radius, 0.15 m outer radius copper solenoid, situated surrounding the central TFC stack. The solenoid comprises 240, 11 × 11 mm, square cross-section solid copper windings, with convective cooling provided through an air-flow introduced into the central stack. Thermal stresses induced through component heating limit the solenoid to a 70° K temperature increase during operation, resulting in an effective maximum magnetic flux swing of ≈ 260 mWb, comparing well to other similarly sized machines [25,38,39]. Plasma breakdown is assisted via a pre-ionisation step employing 6 kW of microwave heating, and an additional 200 kW of Electron Cyclotron Resonance Heating (ECRH) will be employed in phase 3. The installation of a Neutral Beam Injector (NBI) from phase 2 onwards introduces a further 600 kW (injection energy $E_{inj} = 45$ keV) of plasma heating.

Development of the SMART device will proceed through multiple stages, each representing a significant improvement in the pulse duration, heating power and achievable plasma shaping, the main parameters of which are shown in Table 1. Note that the aspect ratio, major and minor radii shown in Table 1 reflect the baseline equilibrium configuration. The triangularly shaped equilibria exhibit reduced elongation and increased aspect ratio in exchange for significantly increased triangularity, see Section 4.3 for more details.

Phase 1 will initiate first plasma (in hydrogen) and serve as a proof-

Table 1
Key operational parameters of the SMART device for phases 1 - 3.All parameters determined within FIESTA, excepting electron density n_e and temperature T_e, which are provided by ASTRA [40,41].

Parameter	Phase 1	Phase 2	Phase 3
R_{geo} [m]	≥ 0.4	≥ 0.4	≥ 0.4
a_{geo} [m]	≥ 0.2	≥ 0.2	≥ 0.2
A [-]	≥ 1.85	≥ 1.85	≥ 1.70
n_e [m^{-3}]	1×10^{19}	5×10^{19}	1.2×10^{20}
T_e [eV]	120	250	700
κ [-]	≤ 1.95	≤ 2.00	≤ 2.25
δ [-]	±0.40	±0.50	±0.50
B_ϕ [T]	0.10	0.30	1.0
I_p [kA]	30	100	500
τ_{ft} [ms]	20	100	500
P_{ECRH} [kW]	6 (2.45 GHz)	6 (7.5 GHz)	200
P_{NBI} [kW]	-	600	600

of-concept for device diagnostics and operations. Phase 2, along with an increase in toroidal field and plasma current, introduces NBI heating and will demonstrate highly shaped negative and positive triangularities in a low aspect ratio hydrogen plasma. Phase 3 represents a significant increase in toroidal field strength, plasma current and discharge timescale, placing SMART alongside other current-generation machines. Phase 3 also includes an optimisation of the plasma shaping parameters, notably a reduction in the aspect ratio, and an increase in the NBI and ECRH plasma heating. This work focuses on SMART phase 2 and addresses the start-up procedure, plasma breakdown criteria and degree of achievable plasma shaping.

3. Numerical model

A plasma in equilibrium maintains a force balance between the inward current induced $\mathbf{J} \times \mathbf{B}$ force and outward thermal pressure p. In a toroidal geometry this force balance can be numerically defined as a solution to the Grad-Shafranov (GS) equation [42,43]:

$$\nabla^* \psi = -\mu_0 R^2 \frac{dp}{d\psi} - f \frac{df}{d\psi} \tag{1}$$

where ∇^* is the Stokes operator [44]

$$\nabla^* = R \frac{\partial}{\partial R}\left(\frac{1}{R}\frac{\partial}{\partial R}\right) + \frac{\partial^2}{\partial Z^2} \tag{2}$$

In both Eqs. (1) and (2), R and Z refer to the radial and azimuthal coordinates, p is the plasma thermal pressure and $f = RB_\phi$ where both p and f are functions of magnetic poloidal flux ψ, and together describe the toroidal plasma current and toroidal magnetic field profiles. The final equilibrium field is a combination of the vacuum magnetic field, determined by the coil geometric and current configuration, the self-induced magnetic field of the plasma, and additional fields arising from eddy currents in the vessel structure. Reliable modelling of plasma equilibria therefore requires knowledge of the geometric and magnetic topology, time-resolved coil currents and plasma currents. Finally, addressing the plasma breakdown requires modelling of the eddy currents induced during solenoid and coil ramps prior to the discharge, as these significantly impact the null-field (i.e. vacuum) magnetic topology and breakdown criteria [26,45].

To achieve these requirements, three distinct models were utilised within the Fiesta code environment [46–49], providing information on the plasma equilibrium, vacuum field, breakdown and plasma current evolution. The model, an overview of which is presented in Fig. 2, consists of a linear current density model (based upon TOPEOL [50]), a free-boundary axisymetric equilibrium solver (EFIT) [51], and a rigid current displacement circuit equation model (RZIp) [49,52,53].

The simulations are performed on a 2D axisymmetric rectilinear grid, shown previously in Fig. 1(b), containing 300 × 251 ($R \times Z$) cells, corresponding to a radial resolution of 5 mm per cell and an axial resolution of 2.6 mm per cell. The simulation geometry includes the vessel walls, PF and Div coil sets and the central solenoid, all modelled as toroidal current carrying filaments, note that the TFC are not included in the simulation geometry where Fiesta assumes an axisymmetrical toroidal field. The vessel wall, shown in green, is constructed from filaments adhering to the differential wall thicknesses detailed in Section 2, while maintaining a constant cross-sectional area of 0.225 mm^2, a resistivity of 6.9×10^{-7} Ω and density of 7.8×10^3 kgm^{-3}. Treatment of the passive vessel filaments with respect to induced eddy currents is discussed in detail with respect to the RZIp model.

The positions of the PF and Div coils are defined at their geometric centre, however as each coil consists of multiple filaments the extended shape of the coil affects the resultant fields. The coils posses an extended dimension set by the number of windings (in R and Z) and the width and height of each winding. Coil sets PF1, PF2 and Div2 all have six axial windings and four radial windings for a total cross-section of 75 × 50 mm (R,Z), while Div1 has six windings in both directions for a total cross-section of 75 × 75 mm. Finally, the central solenoid is modelled as a linear array of 210 filaments, of axial extent $-0.7750 \leq Z \leq 0.7750$ m and radial extent $0.115 \leq R \leq 0.145$ m, with a geometric centre corresponding to $R = 0.134$ m.

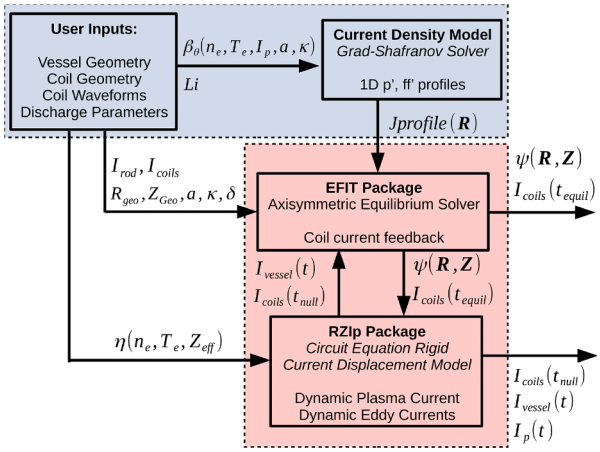

Fig. 2. Overview of numerical model. Initial conditions are denoted in blue, while iterated procedures are highlighted in red. Parameters: plasma density n_e, electron temperature, T_e, plasma current I_p, solenoid inductance L_I, central rod current I_{rod}, Solenoid, PF and Div coil set current waveforms I_{coils}, plasma resistivity η, effective ion charge Z_{eff}, radial plasma current profile $J_{profile}(\mathbf{R})$ and poloidal magnetic flux $\psi(\mathbf{R}, \mathbf{Z})$, where time dependant variables are specified over the full discharge t, or at a specific time corresponding to the flat-top (t_{equil}) or vacuum (t_{null}) configurations. Plasma shaping parameters: R_{geo}, Z_{geo}, minor radius, a, elongation, κ and triangularity δ. (For interpretation of the references to colour in this figure legend, the reader is referred to the web version of this article.)

All simulated discharges utilise phase 2 operating conditions, (see Table 1), employing a toroidal field of $B_\phi = 0.3$ T and a flat-top plasma current of 100 kA. The line-averaged flat-top plasma density was set to $n_e = 1.64 \times 10^{19}$ m^{-3} (assuming a Greenwald fraction $n_e/n_G \approx 0.40$, where $n_G = I_p/\pi a^2$ is the Greenwald density limit [54]), while the corresponding line-averaged flat-top electron and ion temperatures were set to 250 eV and 75 eV, respectively. The conservative values employed for plasma density and ion temperature represent a conservative estimate for phase 2 operation employing low-to-moderate NBI powers, based upon ASTRA [40,41] simulations.

Given the input geometry and discharge parameters, two methods were employed to obtain plasma equilibria, denoted as the 'forward' and 'inverse' methods. The 'forward' method employs p' and ff' coefficients, differentiated with respect to the poloidal flux function, to specify the plasma current density profile $J_{profile}(\mathbf{R})$ at time t, while boundary conditions are set by the instantaneous Sol, PF and Div coil currents in I_{coils}. In the absence of a plasma this method can also be utilised to compute the vacuum field topology, as employed for analysis of the null-field prior to breakdown in Section 4.2. The 'inverse' method (EFIT) takes a pre-computed plasma current density profile at time τ, estimated from β_θ, and returns an optimised equilibrium $\psi(R, Z)$ for a given set of target plasma shaping parameters, R_{geo}, Z_{geo}, a, κ and δ, as well as the coil current boundary conditions I_{coils} required to achieve the target geometry. The pre-computed plasma current density profile is obtained via a linear model (based upon TOPEOL) employing an estimated β_θ to obtain p' and ff', where β_θ is computed from the flat-top discharge conditions by Eq. (3):

$$\beta_\theta = 3\mu_0 e n_e \kappa \frac{(T_e + T_i)}{\left(\mu_0 I_p / 2\pi a\right)^2} \tag{3}$$

Here, μ_0 is the vacuum permittivity, e is the elementary charge, n_e is

the plasma density, I_p is the plasma current, T_e and T_i are the electron and ion temperatures, respectively, while a is the plasma minor radius and κ is the plasma elongation. Notably, this method requires providing initial 'guesses' for the PF and Div coil currents, as well as the optimised equilibrium minor radius a and elongation κ. These initial inputs were manually modified until the input minor radius and elongation matched those of the optimised EFIT equilibrium, ensuring agreement between the input and optimised β_θ.

The time-resolved vessel, coil and plasma current evolution is obtained from the RZIp package, which computes induced currents based on a rigid circuit displacement model [49,52,53]. RZIp considers the discretised vacuum vessel, coil and solenoid filaments and assigns them each with an equivalent resistance and inductance based upon the input conditions and geometry. Currents induced within each coil and vessel filament can then be obtained through a matrix application of Ohm's law:

$$\underline{\underline{\mathscr{M}}}\frac{d\mathbf{I}}{dt} + \underline{\underline{\mathscr{R}}}\mathbf{I} = \mathbf{V} \tag{4}$$

where, $\mathscr{M}$ is a symmetric square matrix whose diagonal elements contain the self-inductance of the coil and vessel elements, and whose triangular elements contain the mutual coil-to-coil, vessel-to-vessel and coil-to-vessel inductance between all filaments; $\mathscr{R}$ is a diagonal matrix containing the resistance of each filament; while $\mathbf{I}$ and $\mathbf{V}$ are vector arrays containing the time varying filament currents and voltages, respectively. In this fashion, supplying the simulation geometry, material resistances and time resolved coil current waveforms is sufficient to compute the vacuum circuit, returning time-resolved currents and voltages for each filament.

Inclusion of the plasma within the model is achieved through considering the plasma column as a rigid toroidal circuit with a fixed cross-section and current density profile, in essence modeling the plasma as an extended filament. The mutual inductance between the plasma circuit and the coil and vessel filaments is updated between iterations such that small radial and horizontal movements in response to $J \times B$ forces are allowed. Plasma resistivity is determined via a Spitzer model assuming an effective charge of $Z_{eff} = 2.0$, accounting for carbon impurities sputtered from the inboard tiles during operation [35]. The time transient plasma current I_p and loop voltage V_p therefore naturally result from the circuit model in response to changes in the coil and vessel filaments. Further, eddy currents induced from changes to the plasma current, and subsequent effects arising from those eddy currents, are also implicitly accounted for within the model. Employing these components, a typical simulation consists of the following steps:

1) The TOPEOL solver is employed to compute a plasma current density profile utilizing input parameters β_θ, L_i, I_{rod} and I_p corresponding to the plasma current flat-top portion of the discharge.

2) The EFIT model is employed to determine PF and Div coil currents employing the supplied plasma current density profile, while attempting to match the target input shaping parameters (R_{geo}, Z_{geo}, a_{geo}, κ and δ). In the first iteration, vessel eddy currents are set to zero.

3) The RZIp model is employed in conjunction with a vacuum field solver to optimise the null-field magnetic topology, such that the poloidal magnetic field B_θ on-axis is minimised, returning the required PF and Div coil currents. In the first iteration, vessel eddy currents are set to zero.

4) The RZIp model is employed with the discharge equilibrium shape computed in step 2, and the associated PF and Div coil waveforms computed in steps 2 and 3, to extrapolate the time-resolved plasma and vessel eddy currents from plasma breakdown through to the end of the discharge.

5) Steps 2 and 3 are repeated to obtain the final optimised null-field and flat-top discharge equilibria employing both: the updated EFIT PF and Div coil currents computed in steps 2 and 3, and the vessel eddy currents computed in step 4.

This paper focuses on the phase 2 of SMART development, employing target operational conditions achievable following the initial commissioning and testing in phase 1. Equilibria are computed at two time points within the discharge; a null-field configuration, computed immediately preceding breakdown, and a steady-state discharge equilibrium, computed during the plasma current flat-top. The former of these is presented in Section 4.2 with relation to plasma breakdown and start-up procedures, while the latter are introduced in Section 4.3, including a discussion on the degree of achievable plasma shaping. However, before presenting these equilibria, an overview of the PFC and Div current waveforms employed to achieve them is presented in Section 4.1.

4. SMART phase 2 operation

4.1. Typical discharge procedure

Thermal considerations due to ohmic losses and power supply stability place strict constraints on the design of the solenoid current waveform and the length of the discharge [37]. These constraints must be balanced against the requirements for breakdown and the target equilibrium conditions, $I_p, R_{geo}, a, \kappa, \delta$. As such, modelling of representative start-up and discharge procedures play a key role in the design of the PF and Div coil sets.

Predicted discharge procedures for SMART have been developed employing the model described in Section 3. The temporally resolved Sol, PF and Div coil current waveforms for the phase 2 baseline case (see Fig. 6(b)) are shown in Fig. 3(a), while the associated plasma current and net vessel eddy current are presented in Fig. 3(b), and the loop voltage induced via the solenoid is shown in Fig. 3(c).

The full discharge procedure for the phase 2 baseline scenario, shown in Fig. 3(a), comprises four stages: a null-field stage between $t = -20$ ms to $t = 0$ ms, denoted blue, a breakdown and burn-through stage between $t = 0$ ms to $t = 15$ ms, denoted red, a transition stage

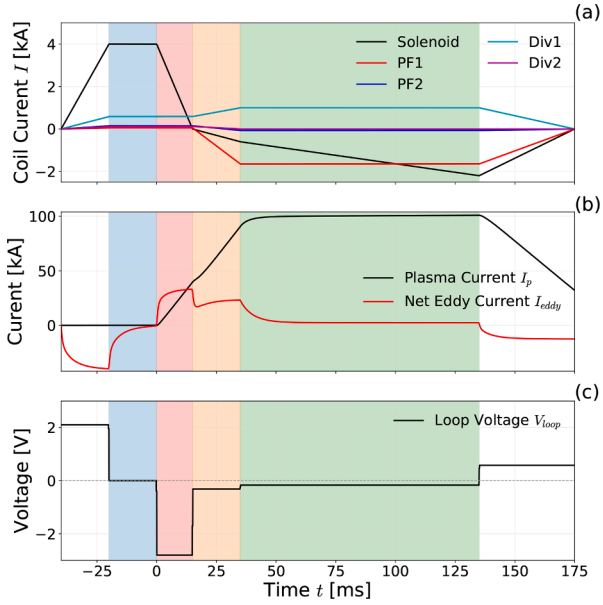

Fig. 3. Time history of the phase 2 baseline discharge, showing the (a) Sol, PF and Div coil current waveforms and (b) the time-resolved plasma current. Operational stages consist of a null-field stage between $t = -20$ ms to $t = 0$ ms, denoted blue, a breakdown and burn-through stage between $t = 0$ ms to $t = 15$ ms, denoted red, a transition stage between $t = 15$ ms to $t = 35$ ms, denoted orange, and the flat-top discharge stage from $t = 35$ ms to $t = 135$ ms, denoted green. Operating Conditions: $I_p = 100$ kA, $B_\phi = 0.3$ T, $\tau_{ft} = 100$ ms. (For interpretation of the references to colour in this figure legend, the reader is referred to the web version of this article.)

between $t = 15$ ms to $t = 35$ ms, denoted orange, and the flat-top discharge stage from $t = 35$ ms to $t = 135$ ms, denoted green.

Stage 1 initiates with the solenoid, PF and Div coils ramping into their optimised null-field configuration from $t = -40$ ms to $t = -20$ ms. The particular configuration of PF and Div coil currents is designed to minimise the on-axis poloidal magnetic field $\mathbf{B}_\theta$ as required for ohmic breakdown, see Section 4.2 for more details. The optimised null-field is maintained for a further 20 ms until $t = 0$ ms to allow time for eddy currents to decay, shown in Fig. 3(b).

Stage 2 begins at $t = 0$ ms with a steep initial solenoid ramp from 4000 A to 0 A (-266 A/ms) between $t = 0 - 15$ ms, designed to maximise the solenoid induced breakdown loop voltage, shown in Fig. 3(c). The PF and Div coil currents maintain their null-field configuration until the end of the initial solenoid ramp, as such the loop voltage V_{loop} induced is uniquely defined by the solenoid ramp and can be computed as shown in Eq. (5).

$$V_{loop} = A_{sol}\frac{\mu_0 \dot{I}_{Sol} N_{Sol}}{L_{Sol}} \tag{5}$$

Where, $\dot{I}_{Sol}$ is the rate of change of solenoid current with respect to time, $N_{Sol} = 240$ is the number of solenoid windings, $L_{Sol} = 1.55$ m is the solenoid length, A_{Sol} is the solenoid cross-sectional area and μ_0 is the vacuum permeability. From this, the induced toroidal electric field can also be computed as $E_\phi = V_{loop}/L_\phi$ where $L_\phi = 2\pi R$ is the toroidal path length at any given radius R. A maximum loop voltage of $V_{loop} = 2.8$ V is induced, resulting in breakdown occurring within 3 ms following ramp-down, the details of which are discussed in Section 4.2. Following breakdown, the plasma current grows at $\approx$ 3.5 MA/s, coinciding with the induction of eddy currents in the vessel structure, both shown in Fig. 3(b). By the end of the initial solenoid ramp-down at $t = 15$ ms the induced eddy current reaches a vessel averaged value of $\approx$ 40 kA, primarily located within the inboard vessel wall adjacent to the solenoid [36].

Stage 3 is a transitional stage from $t = 15 - 35$ ms where the PF and Div coils swing into their discharge configuration. The solenoid executes a secondary intermediate ramp from 0 A to -600 A (-40 A/ms) until $t = 30$ ms, maintaining a plasma current growth of $\approx$ 3.0 MA/s as required to reach the target flat-top plasma current of 100 kA. Net vessel eddy currents reduce to $\approx$ 20 kA, primarily situated adjacent to the outboard midplane and vessel caps, being induced via the PF1 and Div1 coil sets.

Stage 4 represents the main discharge phase, lasting for $\tau_{ft} = 100$ ms between $t = 35 - 135$ ms where the plasma current and shaping parameters have reached their target values. The PF and Div coil sets maintain the discharge configuration, while the solenoid continues into a final shallow tertiary solenoid ramp from -600 A to -2200 A (-16 A/ms), maintaining a constant flat-top current of $I_p = 100$ kA. Plasma current decay arises from both internal resistive losses, where $\eta_p = 4.6 \times 10^{-7}$ [Ω m^{-1}], for $Z_{eff} = 2$, and inductive losses to the vessel walls through the RZIp model, see discussion surrounding Eq. (4).

Following stage 4, the solenoid and all coil sets are ramped to zero current and the plasma decays within $\approx$ 50 ms. Depending upon the target equilibrium shape, the precise configuration of the PF and Div coil currents changes for stages 3 and 4; however, the optimised null-field and start-up procedure (stages 1 and 2) remain similar for all phase 2 discharges.

4.2. Breakdown

SMART is capable of non-inductive breakdown via a dedicated ECRH pre-ionisation system, however standard operation of SMART is expected to employ a traditional inductive breakdown for reliability. Ohmic breakdown of plasmas is generally described via Townsend avalanche theory [55], and more specifically the Lloyd criterion for magnetised plasmas [56], which states that the minimum electric field E_{bd} required for breakdown of hydrogen or deuterium gas at pressure P (Torr) can be estimated as Eq. (6).

$$E_{bd} = \frac{1.25 \times 10^4 P}{\ln(510 P L_c)} \tag{6}$$

where L_c is the connection length [26,45], defined:

$$L_c = 0.25 a_{eff}\left(\frac{B_\phi}{B_\theta}\right) \tag{7}$$

Here, a_{eff} is the effective minor radius, defined as the distance between R_{geo} to the closest vessel wall, while B_θ and B_ϕ denote the vacuum (null-field) poloidal and toroidal magnetic field strengths, respectively. The connection length physically represents the helical field-line path between two points separated by a straight line path of length a_{eff}, and therefore functions as the maximum distance a particle may be accelerated over, with respect to the traditional Paschen Pd diagram.

In addition to Eq. (6), two empirically validated formulae are widely employed as metrics for reliable breakdown, where Eq. (8) refers to discharges employing pre-ionisation [57] and Eq. (9) refers to purely ohmic discharges [58,59].

$$E_\phi \frac{B_\phi}{B_\theta} \geq 100 \qquad [\mathrm{Vm}^{-1}] \tag{8}$$

$$E_\phi \frac{B_\phi}{B_\theta} \geq 1000 \qquad [\mathrm{Vm}^{-1}] \tag{9}$$

From Eqs. (6), (7) and (9), it can be seen that, for a given operational pressure range, the required electric field for ohmic breakdown is reduced by minimising B_θ. This is achieved through configuring the PF and Div coil currents such that the vacuum magnetic field is minimised prior to solenoid ramp-down, forming a null-field region on-axis, as discussed previously with respect to Fig. 3(a). Optimisation of this null-field is performed by RZIp, accounting for the eddy currents induced in the vessel due to the initial solenoid ramp-up.

Figure 4 (a) shows the optimised null-field B_θ at time $t = 0$ ms for the phase 2 baseline discharge shown previously in Fig. 3(a), while Fig. 4(b) and (c) show 2D maps of the breakdown metric described by Eq. (9), and connection lengths attained through field-line tracing within the vacuum vessel, respectively.

The poloidal magnetic topology in Fig. 4(a) exhibits a relatively homogeneous 'D-shaped' region where $B_\theta \approx 2$ G, situated between $-0.4 \leq Z \leq +0.4$ and $0.2 \leq R \leq 0.7$, centred on R_{geo}. This zone is bordered by six approximately equidistant B_θ minima, which represent magnetic cusps at points where the field induced by adjacent coils diverges. While of note, these minima are likely spatially unstable and temporally transient during the solenoid ramp-down and are therefore not considered when computing breakdown criteria. Instead, a null-field zone of size 25 cm by 25 cm and centred on the inboard last closed flux surface (LCFS), is defined within the central poloidal field plateau, denoted by the white dashed lines. For the purposes of calculation, breakdown criteria (B_θ, L_c, τ_{bd}) are averaged over this 6.25 cm^2 region as it represents the location of minimum average poloidal magnetic field during the initial solenoid ramp-down. Note, this null-field region does not represent a physical boundary, rather a convenient nomenclature for discussion of breakdown characteristics. Beyond the central plateau there exists a discontinuity in the magnetic topology at the vessel walls, particularly visible at the outboard mid-plane wall, between the PF1 coil set, and arising due to eddy currents induced during the initial solenoid ramp-up into the null-field configuration.

From the null-field magnetic topology it is possible to compute both the breakdown metric (described by Eq. (9)), and the spatially resolved connection length, shown in Fig. 4(b) and (c), respectively. From Fig. 4 (b) it can be seen that the breakdown metric is highest immediately adjacent to the inboard vessel wall. This arises partly from the increased B_ϕ, and partially from the reduced toroidal path length, which increases the toroidal electric field strength, the radial profile of which is

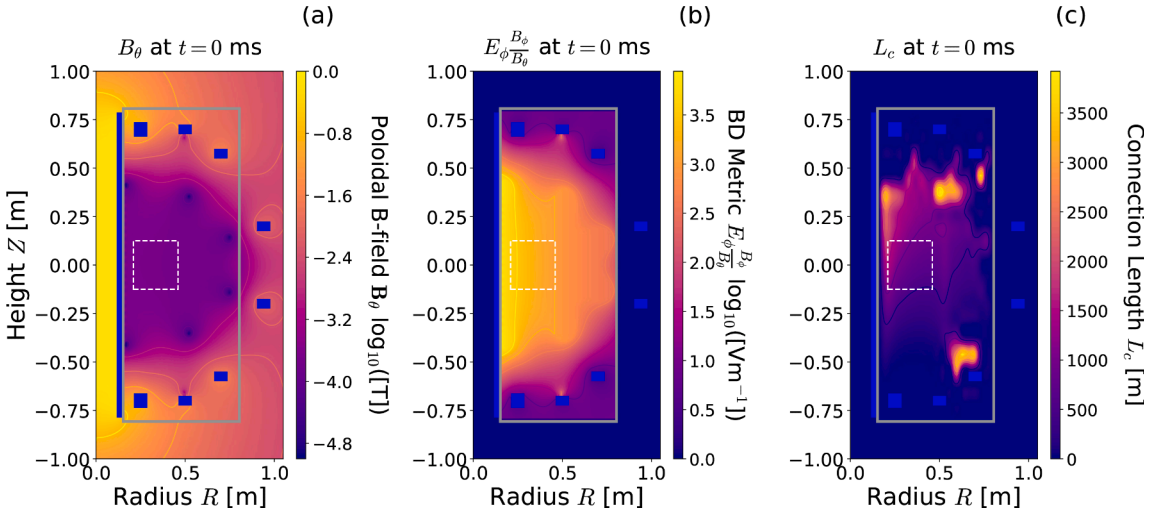

Fig. 4. Contour plots of (a) the phase 2 baseline optimised null-field B_θ, (b) the empirical breakdown metric $E_\phi \frac{\mathbf{B}_\phi}{\mathbf{B}_\theta}$ and, (c) the spatially resolved connection length L_c obtained via field-line tracing. All data presented in panels (a-c) is computed prior to the initial solenoid ramp-down at $\tau = 0$ ms. The vacuum vessel is denoted in grey, coils and solenoid in blue and the 25 $\times$ 25 cm null-field region is denoted by the white dashed box. Operating Conditions: $I_p = 100$ kA, $B_\phi = 0.3$ T, $\tau_{ft} = 100$ ms. (For interpretation of the references to colour in this figure legend, the reader is referred to the web version of this article.)

computed from the maximum loop voltage as described previously in Fig. 3(c).

A generally similar trend can be observed in Fig. 4(c), where connection lengths decrease with increasing radius, again due to reducing B_ϕ. In addition there also exists an asymmetry about the mid-plane with generally longer connection lengths above $Z = 0.0$ m. This asymmetry arises due to the vertical B-field being aligned in the $-Z$ direction, resulting in a net downwards drift in the connection length path, and hence longer lengths for paths starting in the upper portion of the vacuum vessel. These trends are further punctuated by three localised regions of high connection length ($L_c \geq 3000$ m) situated adjacent to the PF2 coils. The largest of these structures at $R = 0.6$ m, $Z = 0.4$ m coincides with a B_θ minima in Fig. 4(a) and as such, is a spatio-temporally transient feature. The smaller structures at $R = 0.7$ m, $Z = -0.5$ m do not correspond to B_θ minima, but instead represent connection paths which form helical trajectories around the PF2 coils, negating the axial or radial drifts. Such paths are only stable in the absence of collisions and for a steady-state B_θ, and therefore also represent transient features.

Accounting for the results presented in Fig. 4(b) and (c), breakdown is most likely to occur on the inboard side of the vessel above the mid-plane, near $R = 0.2$ m, $Z = 0.4$ m. Note however, that these figures represent the upper limits for both the breakdown metric and connection length as they utilise null-field conditions prior to the solenoid ramp-down. During ramp-down, the rapidly changing solenoid current and subsequent eddy currents induced within the inboard wall result in an increased $\mathbf{B}_\theta$, leading to increased connection lengths and reduced breakdown metrics. Averaging the breakdown metric within the null-field region provides an estimated value of $E_\phi \frac{B_\phi}{B_\theta} = 3358$ Vm^{-1}, safely exceeding the minimum threshold for ohmic breakdown by a factor of 3. Performing the same procedure for the connection length within the null-field region via Eq. (7) yields a mean connection length of $L_c = 100.5$ m, agreeing with other similarly sized machines. For the purposes of reliability and safety, these lower null field region averaged values are employed in Section 4.2, ensuring conservative operational estimates.

From the null-field averaged $\mathbf{B}_\theta$ and L_c extracted from Fig. 4(a) and the maximum V_{loop} presented in Fig. 3(a), it is now possible to estimate the expected operational range for SMART phase 2. Fig. 5 shows the Paschen breakdown curve and associated avalanche timescales for SMART phase 2, where the maximum achieved E_{loop} is computed as the maximum induced V_{loop} over a circular path length at the inboard LCFS,

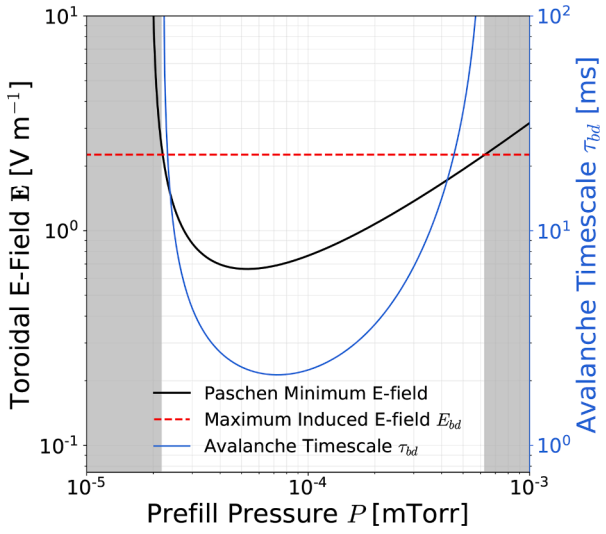

Fig. 5. Phase 2 baseline breakdown criteria illustrating the Paschen breakdown curve in black, computed employing $L_c = 100.5$ m, and corresponding avalanche timescale in blue. The maximum induced toroidal electric field during the initial solenoid ramp-down $E_{loop} = 2.26$ Vm^{-1} is denoted by the red dashed lines. Pressures for which breakdown is not possible are denoted by the greyed out regions. Operating Conditions: $I_p = 100$ kA, $B_\phi = 0.3$ T, $\tau_{ft} = 100$ ms. (For interpretation of the references to colour in this figure legend, the reader is referred to the web version of this article.)

where $R = 0.21$ m.

The Paschen curve in Fig. 5 is calculated employing the null-field averaged connection length of $L_c = 100.5$ m, and exhibits an absolute Paschen minimum field of 0.68 Vm^{-1}. This is safely below the previously calculated toroidal E-field $E_{loop} = 2.26$ Vm^{-1}, shown by the red dashed line, and computed from the maximum induced loop voltage $V_{loop} = 2.8$ V at the centre of the null-field region ($R = 0.21$ m). From this comparison, SMART phase 2 is predicted to possess an operational range of between $3 \leq P \leq 83$ mPa ($0.02 \leq P \leq 0.63$ mTorr), with an optimal pressure of 7 mPa (0.05 mTorr).

While the Paschen minimum is indeed achieved, to achieve breakdown the E-field must be sustained for a suitable timescale such that electron avalanche may proceed to completion. This avalanche time-

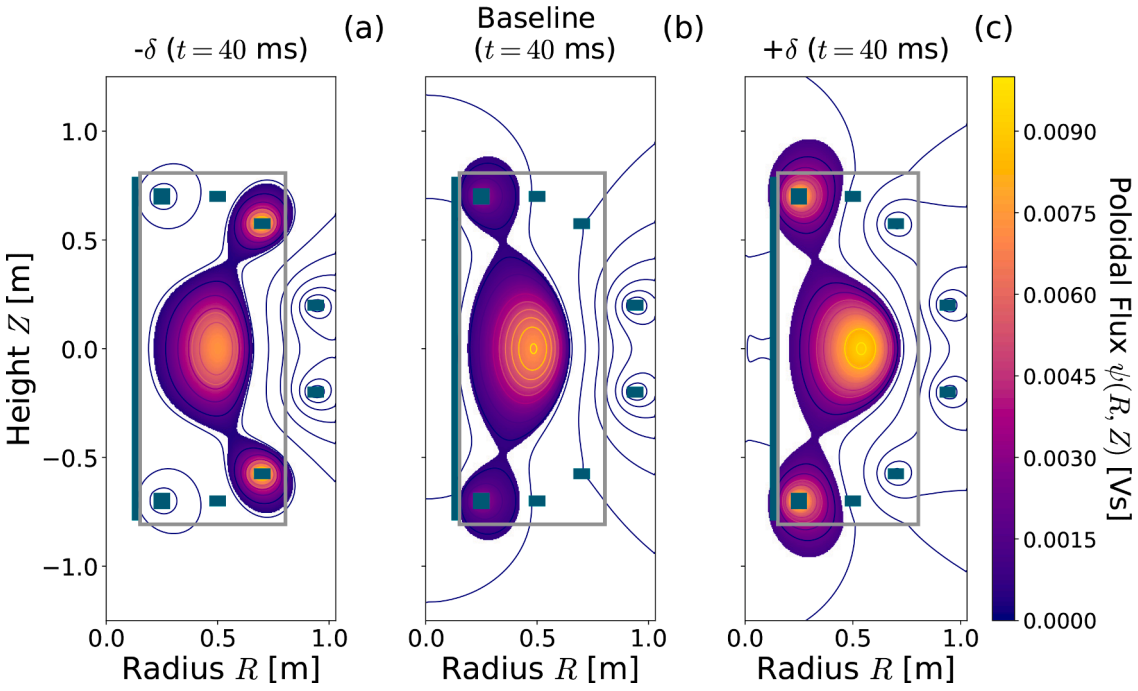

Fig. 6. Phase 2 discharge equilibria, (a) employing negative triangularity ($\delta = -0.50$, $\kappa = 1.75$, $A = 1.97$), (b) employing baseline configuration ($\delta = +0.20$, $\kappa = 2.00$, $A = 1.85$) and (c) employing positive triangularity ($\delta = +0.47$, $\kappa = 1.51$, $A = 1.85$). All equilibria are computed during the plasma current flat-top at $t = 40$ ms (see Fig. 3). The vacuum vessel is denoted in grey, while coils and solenoid are shown in teal. Operating Conditions: $I_p = 100$ kA, $B_\phi = 0.3$ T, $\tau_{ft} = 100$ ms. (For interpretation of the references to colour in this figure legend, the reader is referred to the web version of this article.)

scale τ_{bd} can be estimated through considering the evolution of the electron density during the avalanche [56], and is computed as:

$$\tau_{bd} = \frac{ln(n_{bd}/n_{e0})}{V_{De}(\alpha - 1/L_c)} \tag{10}$$

Here, $n_{e0} = 1\ \mathrm{m}^{-3}$ is the initial background electron density, n_{bd} is the electron density at the 'completion' of breakdown, $V_{De} = \eta E_{loop}/P$ is the electron drift velocity, where $\eta \approx 43$, and α is the 1st Townsend coefficient given by:

$$\alpha = A_T P \cdot exp\left(\frac{B_\phi P}{E_{loop}}\right) \tag{11}$$

where $A_T = 510\ \mathrm{m}^{-1}\mathrm{Torr}^{-1}$ and $B_\phi = -1.25 \times 10^4\ \mathrm{Vm}^{-1}\mathrm{Torr}^{-1}$ for deuterium plasma discharges [45], with previous work showing that these values of A_T and B_ϕ also hold to within 2% for hydrogen discharges [56], as employed in SMART phases 1 and 2. For the τ_{bd} profile shown in Fig. 5, an electron density of $n_{bd} = 0.15 n_e$ (where n_e is as computed from the Greenwald limit) was chosen to mark the 'completion' of breakdown. This density represents a reasonable estimate for the density at which the electron-ion collision frequency exceeds the electron-neutral collision frequency [56]. Note however, that the target electron density was maintained constant for varying prefill pressure and as such the breakdown densities n_{bd} and avalanche timescales at lower pressures likely represent a slight overestimation.

Given these conditions, the avalanche timescales computed for SMART phase 2 range over three orders of magnitude, achieving a minimum of $\tau_{bd} = 2.13$ ms for a prefill pressure of 0.07 mTorr, slightly higher than the optimum pressure suggested by the Paschen minimum alone. Notably, an avalanche timescale of between $2 - 3$ ms is significantly below the initial stage 2 solenoid ramp-down timescale of 15 ms, providing adequate time for breakdown and burn-through of the remaining neutral species to occur.

4.3. MHD equilibria and shaping

Following breakdown, the plasma current grows at a rate of ≥ 3.0 MA/s, reaching the target flat-top current of 100 kA by $t = 35$ ms as shown previously in Fig. 3(b). Flat-top discharge equilibria are computed at time $t = 40$ ms, allowing for stabilisation of the plasma and vessel eddy currents following the PF and Div coil swings. Figures 6(a-c) present equilibria demonstrating the range of plasma shaping achievable within SMART phase 2, including: a negative triangularity configuration ($\delta = -0.50$), a baseline configuration ($\delta = +0.20$), and a positive triangularity configuration ($\delta = +0.44$), respectively.

The baseline equilibrium, shown in Fig. 6(b), represents the prospective 'standard' phase 2 discharge configuration; designed to minimise the aspect ratio ($A = 1.85$) and maximise the elongation ($\kappa = 2.00$), with a moderately positive triangularity ($\delta = 0.20$). The highly elongated shape offsets the reduced aspect ratio, resulting in a moderate plasma volume of 0.8 m^3, filling approximately 46% of the usable internal volume, accounting for the internal PF and Div coil radial and axial limits. Further, the low aspect ratio enforces a higher average B_ϕ across the plasma, leading to a higher average magnetic helicity (B_ϕ/B_θ) and resulting in a relatively high edge safety factor of $q_{95} = 6.6$.

In addition to the baseline case, two further highly shaped equilibria were developed, shown in Fig. 6(a) and (c), outlining the most negative and most positive triangular discharge configurations achievable within the constraints of the coil geometry and phase 2 power supply limits. Aligning with the SMART mission goals, design priority was given to optimising for the triangular configurations, achieving a minimum negative triangularity of $\delta = -0.50$ and a maximum positive triangularity of $\delta = +0.47$. Beyond these values no stable equilibria were obtained within the PF and Div coil current limitations. In both cases, enhanced triangularity was achieved at the cost of reduced elongation, where $\kappa = 1.50$ for the $+\delta$ case and $\kappa = 1.75$ for the $-\delta$ case, arising from the increased current in the Div1 or PF2 coil sets, respectively. While these reductions in elongation result in reduced minor radii, this is accompanied by an increased R_{geo}; maintaining an aspect ratio of $A =$

1.85 for the $+\delta$ case, while the $-\delta$ case exhibits an increased aspect ratio of $A = 1.97$ due to R_{geo} increasing faster than a. Finally, both shapes exhibit edge safety factors lower than the baseline configuration, arising due to the reduced average B_ϕ across the plasma. This effect is most pronounced in the safety factor $q_{95} = 4.3$ for the $-\delta$ configuration, as compared to $q_{95} = 5.7$ for the $+\delta$ configuration.

A major advantage of the SMART device, with regards to plasma shaping, arises from the flexibility in the positioning of the primary shaping coil sets (PF2 and Div1). While representing a greater engineering challenge, the decision to place the primary shaping coils within the vacuum vessel greatly reduces the coil current requirements to achieve the above highly-shaped equilibria. As the current requirements on the PF1 coil set are significantly lower than the other coil sets it may remain external to the vessel, increasing the internal volume and reducing the poloidal ripple. An analysis of the SMART device in which all coils were external to the vessel has shown unacceptably high current demands on the Div1 and PF2 coil sets, while simultaneously predicting reduced shaping parameters. Finally, it was found that the axial separation of the internal PF2 coil set significantly impacted the degree of achievable negative triangularity. Enhanced negative triangularities were achieved primarily through reducing the axial separation of the PF2 coil set, which form the $-\delta$ X-points, as compared to the Div1 coil set which form the $+\delta$ X-points. This enabled 'sharper' $-\delta$ X-points and 'flatter' outboard flux surfaces as compared to the positive triangularity cases.

The shaping characteristics presented in Fig. 6(a–c) in combination with the operational parameters shown previously in Table 1 place the expected capabilities of SMART phase 2 in line with previous generation small-to-mid size spherical tokamaks. SMART phase 3 aims to expand upon these capabilities, through improvements to the central solenoid and PFC power supplies, and will be capable of achieving triangularities in excess of ± 0.5 for operating conditions of $B_\phi = 1$ T, $I_p = 500$ kA and $\tau_{ft} = 500$ ms. The unique capability to achieve such highly shaped plasmas within a spherical tokamak, in particular negative triangularies, will enable quantification of the MHD stability, radial transport, and edge physics in high β plasmas, ensuring that SMART directly contributes to prospective future commercial spherical tokamak projects.

5. Conclusions

Two-dimensional axisymmetric simulations of the discharge procedures and target shaped equilibria in the novel *SMall Aspect Ratio Tokamak* (SMART) device have been performed employing the Fiesta toolbox. This work focused on phase 2 of the SMART design process, representing the first stage capable of highly-shaped plasma configurations. Three prospective phase 2 discharge configurations were examined; a baseline configuration for which the aspect ratio (A = 1.85) is minimised and the elongation is maximised ($\kappa = 2.07$) and a pair of highly triangular configurations, achieving triangularities in the range $-0.50 \leq \delta \leq +0.47$ for a 100 kA plasma column. Modelling of the baseline configuration start-up procedure and discharge configuration was performed, including a self-consistent consideration of induced vessel eddy currents through a rigid current displacement model (RZIp). A maximum loop voltage of $V_{loop} = 2.8$ V was achieved for a solenoid ramp of 4 kA, in the absence of pre-ionisation. Analysis and optimisation of the pre-ramp null-field configuration estimated connection lengths of $\approx$ 100 m, corresponding to an operational prefill pressure range of between $3 \leq P \leq 83$ mPa ($0.02 \leq P \leq 0.63$ mTorr), with an optimal pressure of 7 mPa (0.05 mTorr). Further analysis of the Townsend breakdown for these conditions revealed a minimum avalanche timescale of 2.12 ms, significantly below the 15 ms start-up timescale, demonstrating the capacity for purely ohmic breakdown in the SMART device. The highly shaped configurations and discharge thresholds presented here represent the potential for SMART to produce many high impact contributions to spherical tokamak research, including transport and edge stability studies. Looking forward, continued modelling and development of the SMART device aims to improve upon these targets, while enabling the training of the next generation of fusion engineers and physicists.

Declaration of Competing Interest

The authors declare that they have no known competing financial interests or personal relationships that could have appeared to influence the work reported in this paper.

Acknowledgements

The authors would like to thank the VEST team for their technical and engineering support. This work received funding from the Fondo Europeo de Desarollo Regional (FEDER) by the European Commission under grant agreement numbers IE17-5670 and US-15570. In addition support from the European Research Council (ERC) under the European Union's Horizon 2020 research and innovation programme (grant agreement No. 805162) is gratefully acknowledged.

References

[1] B.G. Hong, Y.S. Hwang, J.S. Kang, D.W. Lee, H.G. Joo, et al., Conceptual design study of a superconducting spherical tokamak reactor with a self-consistent system analysis code, Nucl. Fusion 51 (11) (2011) 113013, https://doi.org/10.1088/0029-5515/51/11/113013.
[2] R.J. Akers, A. Bond, R.J. Buttery, P.G. Carolan, G.F. Counsell, et al., Steady state operation of spherical tokamaks, Nucl. Fusion 40 (6) (2000) 1223–1244, https://doi.org/10.1088/0029-5515/40/6/317.
[3] Y.K. Peng, D.J. Strickler, Features of spherical torus plasmas, Nucl. Fusion 26 (6) (1986) 769–777, https://doi.org/10.1088/0029-5515/26/6/005.
[4] A. Sykes, R.J. Akers, L.C. Appel, P.G. Carolan, J.W. Connor, et al., H-mode operation in the start spherical tokamak, Phys. Rev. Lett. 84 (3) (2000) 495–498, https://doi.org/10.1103/PhysRevLett.84.495.
[5] M. Gryaznevich, R. Akers, P.G. Carolan, T. Erneux, D. Gates, et al., Achievement of record β in the START spherical tokamak, Phys. Rev. Lett. 80 (18) (1998) 3972–3975, https://doi.org/10.1103/PhysRevLett.80.3972.
[6] A. Sykes, G.W. Crawford, G. Cunningham, N.A. Fawlk, D.H. Goodall, et al., START spherical tokamak, Proc. Symp. Fusion Eng. 2 (1995) 1442–1446.
[7] B. Lloyd, J.W. Ahn, R.J. Akers, L.C. Appel, E.R. Arends, et al., Overview of recent experimental results on MAST, Nucl. Fusion 43 (12) (2003) 1665–1673, https://doi.org/10.1088/0029-5515/43/12/012.
[8] A.C. Darke, M. Cox, J.R. Habar, J.H. Hay, J.B. Hicks, et al., The mega amp spherical tokamak, Proc. Symp. Fusion Eng. 2 (1995) 1456–1459.
[9] S.M. Kaye, M.G. Bell, R.E. Bell, S. Bernabei, J. Bialek, et al., Progress towards high performance plasmas in the national spherical torus experiment (NSTX), Nucl. Fusion 45 (10) (2005) S168, https://doi.org/10.1088/0029-5515/45/10/S14.
[10] G.D. Garstka, S.J. Diem, N.W. Eidietis, R.J. Fonck, B.T. Lewicki, et al., The upgraded pegasus toroidal experiment, Nucl. Fusion 46 (8) (2006) S603, https://doi.org/10.1088/0029-5515/46/8/S06.
[11] J.A. Reusch, G.M. Bodner, M.W. Bongard, M.G. Burke, R.J. Fonck, et al., Non-inductively driven tokamak plasmas at near-unity βt in the Pegasus toroidal experiment, Phys. Plasmas 25 (5) (2018) 056101, https://doi.org/10.1063/1.5017966.
[12] V.K. Gusev, N.N. Bakharev, V.A. Belyakov, B.Y. Ber, E.N. Bondarchuk, et al., Review of Globus-M spherical tokamak results, Nucl. Fusion 55 (10) (2015) 104016, https://doi.org/10.1088/0029-5515/55/10/104016.
[13] V.B. Minaev, V.K. Gusev, N.V. Sakharov, V.I. Varfolomeev, N.N. Bakharev, et al., Spherical tokamak Globus-M2: design, integration, construction (2017).
[14] K. Hanada, K. Sato, H. Zushi, K. Nakamura, M. Sakamoto, et al., Steady-state operation scenario and the first experimental result on QUEST, Plasma Fusion Res. 5 (2010) 1–6, https://doi.org/10.1585/pfr.5.S1007.
[15] H. Idei, T. Kariya, T. Imai, K. Mishra, T. Onchi, et al., Fully non-inductive second harmonic electron cyclotron plasma ramp-up in the QUEST spherical tokamak, Nucl. Fusion 57 (12) (2017) 126045, https://doi.org/10.1088/1741-4326/aa7c20.
[16] T. Maekawa, Y. Terumichi, H. Tanaka, M. Uchida, T. Yoshinaga, et al., Formation of spherical tokamak equilibria by ECH in the LATE device, Nucl. Fusion 45 (11) (2005) 1439–1445, https://doi.org/10.1088/0029-5515/45/11/026.
[17] R. Majeski, R.E. Bell, D.P. Boyle, R. Kaita, T. Kozub, et al., Compatibility of lithium plasma-facing surfaces with high edge temperatures in the lithium tokamak experiment, Phys. Plasmas 24 (5) (2017) 056110, https://doi.org/10.1063/1.4977916.
[18] J.C. Schmitt, T. Abrams, L.R. Baylor, L. Berzak Hopkins, T. Biewer, et al., Results and future plans of the lithium tokamak experiment (LTX), J. Nucl. Mater. 438 (SUPPL) (2013) S1096–S1099, https://doi.org/10.1016/j.jnucmat.2013.01.241.
[19] M. Gryaznevich, O. Asunta, Overview and status of construction of ST40, Fusion Eng. Des. 123 (2017) 177–180, https://doi.org/10.1016/j.fusengdes.2017.03.011.

[20] P.F. Buxton, O. Asunta, M.P. Gryaznevich, D. Lockley, S. McNamara, et al., On the design and role of passive stabilisation within the ST40 spherical tokamak, Plasma Phys. Controlled Fusion 60 (6) (2018) 064008, https://doi.org/10.1088/1361-6587/aabd01.

[21] Y. Wang, L. Zeng, Y. He, Initial plasma startup test on SUNIST spherical tokamak, Plasma Sci. Technol 5 (6) (2003) 2017–2022, https://doi.org/10.1088/1009-0630/5/6/001.

[22] Y. He, L. Zhang, L. Xie, Y. Tang, X. Yang, et al., Preliminary experiment of non-inductive plasma current startup in SUNIST spherical tokamak, Plasma Sci. Technol 8 (1) (2006) 84–86, https://doi.org/10.1088/1009-0630/8/1/5.

[23] Y. Takase, A. Ejiri, N. Kasuya, T. Mashiko, S. Shiraiwa, et al., Initial results from the TST-2 spherical tokamak, Nucl. Fusion 41 (11) (2001) 1543–1550, https://doi.org/10.1088/0029-5515/41/11/303.

[24] A. Ejiri, Y. Takase, H. Kasahara, T. Yamada, K. Hanada, et al., RF start-up and sustainment experiments on the TST-2@K spherical tokamak, Nucl. Fusion 46 (7) (2006) 709–713, https://doi.org/10.1088/0029-5515/46/7/003.

[25] K.J. Chung, Y.H. An, B.K. Jung, H.Y. Lee, C. Sung, et al., Design features and commissioning of the versatile experiment spherical torus (VEST) at Seoul National University, Plasma Sci. Technol 15 (3) (2013) 244–251, https://doi.org/10.1088/1009-0630/15/3/11.

[26] K.J. Chung, Y.H. An, B.K. Jung, H.Y. Lee, J.J. Dang, et al., Initial plasma start-up using partial solenoid coils in versatile experiment spherical torus (VEST), Fusion Eng. Des. 88 (6–8) (2013) 787–790, https://doi.org/10.1016/j.fusengdes.2013.02.006.

[27] M.P. Gryaznevich, S.E. Sharapov, Beta-dependence of energetic particle-driven instabilities in spherical tokamaks, Plasma Phys. Controlled Fusion 46 (7) (2004), https://doi.org/10.1088/0741-3335/46/7/S02.

[28] R.J. Akers, J.W. Ahn, G.Y. Antar, L.C. Appel, D. Applegate., et al., Plasma physics and controlled fusion transport and confinement in the mega ampère spherical tokamak (mast) plasma transport and confinement in the mega ampère, Plasma Phys. Controlled Fusion 45 (2003) A175.

[29] W. Guttenfelder, J. Candy, Resolving electron scale turbulence in spherical tokamaks with flow shear, Phys. Plasmas 18 (2) (2011) 022506, https://doi.org/10.1063/1.3551701.

[30] F. Hofmann, O. Sauter, H. Reimerdes, I. Furno, A. Pochelon, Experimental and theoretical stability limits of highly elongated tokamak plasmas, Phys. Rev. Lett. 81 (1998) 2918.

[31] Y. Camenen, A. Pochelon, R. Behn, A. Bottino, A. Bortolon, et al., Impact of plasma triangularity and collisionality on electron heat transport in TCV L-mode plasmas, Nucl. Fusion 47 (7) (2007) 510–516, https://doi.org/10.1088/0029-5515/47/7/002.

[32] C.T. Holcomb, J.R. Ferron, T.C. Luce, T.W. Petrie, P.A. Politzer, et al., Optimizing stability, transport, and divertor operation through plasma shaping for steady-state scenario development in DIII-D, Phys. Plasmas 16 (5) (2009) 056116, https://doi.org/10.1063/1.3125934.

[33] M. Fontana, L. Porte, S. Coda, O. Sauter, The effect of triangularity on fluctuations in a tokamak plasma, Nucl. Fusion 58 (2) (2018) 024002, https://doi.org/10.1088/1741-4326/aa98f4.

[34] K.G. McClements, M.P. Gryaznevich, S.E. Sharapov, R.J. Akers, L.C. Apell, et al., Energetic particle-driven instabilities in the START spherical tokamak physics of energetic particle-driven instabilities in the START spherical tokamak, Plasma Phys. Controlled Fusion 41 (1999) 661–678.

[35] M.E. Austin, A. Marinoni, M.L. Walker, M.W. Brookman, J.S. Degrassie, et al., Achievement of reactor-relevant performance in negative triangularity shape in the DIII-D tokamak, Phys. Rev. Lett. 122 (11) (2019) 115001, https://doi.org/10.1103/PhysRevLett.122.115001.

[36] A. Mancini, J. Ayllon-Guerola, S.J. Doyle, M. Agredano-Torres, D. Lopez-Aires, et al., Mechanical and electromagnetic design of the vacuum vessel of the SMART tokamak, Fusion Eng. Des. 171 (2021) 112542.

[37] M. Agredano-Torres, J.L. Garcia-Sanchez, A. Mancini, S.J. Doyle, J. Ayllon-Guerola, et al., Coils and power supply design for the SMall aspect ratio tokamak (SMART) of the university of seville, Fusion Eng. Des. (2020).In Review

[38] V.K. Gusev, E.A. Azizov, A.B. Alekseev, A.F. Arneman, N.N. Bakharev, et al., Globus-M results as the basis for a compact spherical tokamak with enhanced parameters globus-M2, Nucl. Fusion 53 (9) (2013) 093013, https://doi.org/10.1088/0029-5515/53/9/093013.

[39] V.K. Gusev, T.A. Burtseva, A.V. Dech, G.A. Gavrilov, V.E. Golant, et al., Plasma formation and first OH experiments in the Globus-M tokamak, Nucl. Fusion 41 (7) (2001) 919–925, https://doi.org/10.1088/0029-5515/41/7/313.

[40] G.V. Pereverzev, P.N. Yushmanov, ASTRA–Automated System for Transport Analysis in a Tokamak (IPP 5/98) (2002) 147.

[41] M.G. Sevillano, I. Garrido, A.J. Garrido, Control-oriented automatic system for transport analysis (ASTRA)-Matlab integration for tokamaks, Energy 36 (5) (2011) 2812–2819, https://doi.org/10.1016/j.energy.2011.02.022.

[42] H. Grad, H. Rubin, Hydromagnetic equilibria and force-free fields, J. Nucl. Energy (1954) 7 (3–4) (1958) 284–285, https://doi.org/10.1016/0891-3919(58)90139-6.

[43] V. Shafranov, On magnetohydrodynamical equilibrium configurations, Soviet J. Exp. Theor. Phys. 6 (3) (1958) 545.

[44] H. Zhom, Magnetohydrodynamic Stability of Plasmas, first ed., Wiley-VCH Verlag GmbH, Weinheim, Germany, 2015.

[45] X. Song, X.R. Duan, X.M. Song, G.Y. Zheng, S. Wang, et al., Experimental results of plasma breakdown and flux optimization on HL-2A tokamak, Fusion Eng. Des. 125 (September) (2017) 195–198, https://doi.org/10.1016/j.fusengdes.2017.11.007.

[46] G. Cunningham, High performance plasma vertical position control system for upgraded MAST, Fusion Eng. Des. 88 (12) (2013) 3238–3247, https://doi.org/10.1016/j.fusengdes.2013.10.001.

[47] P.F. Buxton, M.P. Gryaznevich, Merging compression start-up predictions for ST40, Fusion Eng. Des. 123 (2017) 551–554, https://doi.org/10.1016/j.fusengdes.2017.04.067.

[48] L. Kripner, M. Peterka, M. Imr, J. Urban, J. Havl, et al., Equilibrium design for the COMPASS-U tokamak. WDS Annual Conference of Doctoral Students, MATFYPRESS, Prague, 2018, pp. 99–104.

[49] A. Coutlis, I. Bandyopadhyay, J.B. Lister, P. Vyas, R. Albanese, et al., Measurement of the open loop plasma equilibrium response in TCV, Nucl. Fusion 39 (5) (1999) 663–683, https://doi.org/10.1088/0029-5515/39/5/307.

[50] P. Haynes, R.J. Buttery, TOPEOL: A User's Guide edition 2.0. Technical Report, UKAEA Fusion, Culham, UK, 1995.

[51] L.L. Lao, H.S. John, R.D. Stambaugh, A.G. Kellman, W. Pfeiffer, Reconstruction of current profile parameters and plasma shapes in tokamaks, Nucl. Fusion 25 (11) (1985) 1611–1622, https://doi.org/10.1088/0029-5515/25/11/007.

[52] A.S. Sharma, D.J. Limebeer, I.M. Jaimoukha, J.B. Lister, Modeling and control of TCV, IEEE Trans. Control Syst. Technol. 13 (3) (2005) 356–369, https://doi.org/10.1109/TCST.2004.841647.

[53] J.B. Lister, A. Sharma, D.J. Limebeer, Y. Nakamura, J.P. Wainwright, et al., Plasma equilibrium response modelling and validation on JT-60U, Nucl. Fusion 42 (6) (2002) 708–724, https://doi.org/10.1088/0029-5515/42/6/309.

[54] M. Greenwald, Density limits in toroidal plasmas, Plasma Phys. Controlled Fusion 44 (8) (2002) R27, https://doi.org/10.1088/0741-3335/44/8/201.

[55] P.C. De Vries, Y. Gribov, ITER breakdown and plasma initiation revisited, Nucl. Fusion 59 (9) (2019) 096043, https://doi.org/10.1088/1741-4326/ab2ef4.

[56] B. Lloyd, G.L. Jackson, T.S. Taylor, E.A. Lazarus, T.C. Luce, et al., Low voltage Ohmic and electron cyclotron heating assisted startup in DIII-D, Nucl. Fusion 31 (11) (1991) 2031–2053, https://doi.org/10.1088/0029-5515/31/11/001.

[57] Y. An, J. Lee, H. Lee, J. Jo, B.K. Jung, et al., Plasma start-up design and first plasma experiment in VEST, Fusion Eng. Des. 96–97 (2015) 274–280, https://doi.org/10.1016/j.fusengdes.2015.05.015.

[58] Y. Gribov, D. Humphreys, K. Kajiwara, E.A. Lazarus, J.B. Lister, et al., Chapter 8: plasma operation and control, Nucl. Fusion 47 (6) (2007) S385, https://doi.org/10.1088/0029-5515/47/6/S08.

[59] V. Erkmann, U. Gasparino, Electron cyclotron resonance heating and current drive in toroidal fusion plasmas, Plasma Phys. Controlled Fusion 36 (1994) 1869–1962, https://doi.org/10.1088/0741-3335/36/12/001.